R. Schlögel · J.-P. Malet · C. Doubre · T. Lebourg

Structural control on the kinematics of the deep-seated La Clapière landslide revealed by L-band InSAR observations

Abstract The objective of this work is to document the deformation pattern of the deep-seated La Clapière landslide for the period 2007–2010 from the combination of L-band synthetic aperture radar (SAR) interferograms, ground-based total station measurements and identification of the slope geomorphological structures. The interferograms are calculated for pairs of ALOS/PALSAR images at a time interval of 46 days. The displacement field derived from the interferograms reveals a non-uniform displacement gradient from the top (subsidence) to the bottom (accumulation). Vertical velocities are calculated from the unwrapped phase values and are in good agreement with ground-based measurements. The results demonstrate the potential of L-band ALOS/PALSAR imagery for the monitoring of active landslides characterized by complex kinematic patterns and by important changes in the soil surface backscattering in time.

Keywords Landslide · InSAR · ALOS/PALSAR · Displacement monitoring

Introduction

Knowledge on slope surface kinematics is a basic requirement for understanding the controlling mechanisms of landslide deformation. Traditional ground-based approaches (tacheometry, extensometry, GNSS) require a movement velocity above a certain threshold (e.g. centimeters per day) to detect a displacement signal; further, these techniques are time-consuming and costly (mainly in terms of field operations) and give access only to a discrete (e.g. point) information on the movement. As a complement to ground-based measurements, space-borne remote-sensing techniques allow obtaining spatially distributed information on the kinematics of slope movements (Casson et al. 2005).

Techniques using high resolution (HR) to very high resolution (VHR) space-borne optical and radar (SAR) images are able to measure 1D Line-of-Sight (LoS), 2D horizontal and sometimes fully 3D surface displacements. For instance, digital image correlation (DIC) of VHR optical satellite images has been used to estimate the horizontal component of the displacement with a centimetric accuracy (Booth et al. 2013; Stumpf et al. 2014). Over the last decade, in complement to optical images, synthetic aperture radar (SAR) images have become a widely used source of information for landslide detection (Cascini et al. 2009; Lu et al. 2012) and monitoring (Zhao et al. 2012; Raucoules et al. 2013). Comprehensive overviews of SAR observations for landslide investigations have been presented by Colesanti and Wasowski (2006) and Rott and Nagler (2006). However, these reviews predate the launch of the most recent commercial SAR sensors. Rott (2009) provides an updated summary with reference to the TerraSAR-X and COSMO-SkyMed satellites before the availability of the Sentinel constellation (Berger et al. 2012). This recent generation of SAR satellite sensors can acquire, through dedicated

acquisition planning, high-frequency observations (up to every 6 days) over regional areas (e.g. 10–1000 km²) with high resolution (up to 1-m ground resolution).

Two-pass differential InSAR technique (D-InSAR) has been applied for the monitoring of slow-moving landslides (on the order of cm year^{-1}; Massonnet and Feigl 1998; Squarzoni et al. 2003; Schlögel et al. 2015). However, InSAR methods have important limitations associated with geometric and temporal decorrelation, atmospheric artifacts, scale constraints, geometric distortions, a measurement sensitivity limited to a 1D Line-of-Sight (LoS) and average value of measurements for the time window of observation (Colesanti and Wasowski, 2006). A range of techniques has been developed to help minimizing some of these limitations such as time-series analysis (Ferretti et al. 2001; Berardino et al. 2002) or the use of external data to reduce atmospheric path delays (Li et al. 2006; Foster et al. 2013). Analyzing the deformation patterns of large landslides with InSAR is therefore still challenging.

Deep-seated landslides usually involve weathered rock and/or bedrock and consist of large slope failures associated with translational, rotational or complex movement. This type of landslides potentially occurs in tectonic active regions, and the kinematics is controlled by the structures (faults, bedding planes) of the slopes (Dramis and Sorriso-Valvo 1994; Agliardi et al. 2001; Travelletti et al. 2013). They typically move slowly, with displacement rates of a few mm year^{-1} to cm year^{-1} but can occasionally move faster and thus become potentially damaging (Hradecký and Pánek 2008). Specific morpho-structural features such as double ridges, ridge top grabens, concave counterscarps, trenches and steep slopes at the toe characterize this type of landslide (Agliardi et al. 2001).

In the South French Alps, the Argentera-Mercantour mountain range is affected by several deep-seated slope movements. At the mountain range scale, their spatial distribution has been studied through geological field surveys and interpretation of multi-date orthophotographs (Jomard 2006). These investigations concluded on the control of the landslide locations by pre-existing tectonic faults (Guglielmi et al. 2005; Jomard et al. 2007; Bois et al. 2008). At the slope scale, most of the investigations and monitoring were conducted at the La Clapière slope, which is intensively weathered and affected by various sets of discontinuities (Follacci et al. 1988; Follacci, 1999; Gunzburger and Laumonier 2002; Guglielmi et al. 2005). The conclusion of nearly 30 years of displacement monitoring is that there is still limited knowledge on the influence of the fault geometry at depth on the spatial distribution of slope kinematics (Girault and Terrier, 1994; Helmstetter et al. 2004; Delacourt et al. 2004; Delacourt et al. 2007).

In this work, we focus on the kinematic analysis of the deep-seated La Clapière landslide, characterized by a velocity in the order of cm day^{-1} and a complex spatial pattern of displacement. The work is complementary to previous investigations of the slope

kinematics using several techniques (photogrammetry of terrestrial, aerial and satellite optical images, short-wavelength C-band InSAR and on-site total station and GPS periodic measurements) covering various time periods (Girault and Terrier 1994; Fruneau et al. 1996; Casson et al. 2005; Serratrice, 2006).

After presenting the study area, the evolution of the slope surface deformation over the last 30 years and the InSAR processing technique, we analyze L-band SAR images to estimate the displacement field for the period 2007–2010 and compare it to ground-based total station measurements. We focus on the time evolution of the displacement field and identify kinematic and structural sub-units within the landslide body. L-band SAR images proved their usefulness for monitoring such type of active landslides affected by significant changes in the local morphology and the soil surface state modifying the ground scattering properties between two consecutive SAR images.

Geological and geomorphological characteristics of the La Clapière slope

The La Clapière landslide is located in the Tinée valley in the Southeast French Alps, approximately 80 km north of Nizza (Fig. 1a). The active landslide, which is part of a large unstable slope deforming since 3.6 ka (Guglielmi et al. 2005; Lebourg et al. 2010), has been triggered in the early twentieth century (Fig. 1a). In 2014, the landslide has a relative elevation of 750 m (between 1100 and 1850 m a.s.l.) and a volume estimated at 60 million cubic meters (Jomard et al. 2007). The slope is facing the South-West direction (Fig. 1b, c).

The top of the La Clapière landslide corresponds to a 120-m scarp which consists of two lobes (Fig. 1) extending over a width of 800 m at the elevation of 1600 m. The steepest slopes, as well as secondary scarps, are observed at elevation between 1400 and 1500 m corresponding to an outcrop of hard rocks (migmatite and metadiorite) at the 'Barre d'Iglière' (Follacci, 1987). The landslide body is developed in Hercynian rocks composed mainly of weathered and fractured migmatic gneiss (Follacci 1999; Fig. 1c) and overlaps at its base Quaternary alluvial sediments of the Tinée river. The Hercynian-foliated material is dipping sub-horizontally at 5° outside of the landslide body while it is dipping at 10° to 30° within the landslide body (Ivaldi et al. 1991; Gunzburger and Laumonier 2002; Delteil et al. 2003). At the top of the slope, above 1800 m, the metamorphic rocks are weathered over a thickness ranging from 50 to 200 m. In the middle part of the slope and at the toe, the gneiss is fractured (Corsini et al. 1994). Compressive features are observed at the Cascaï thrust that has a N 130° E orientation and dips to the North-East. Extensive features are observed along two main directions:

– a N 110–140° E set of discontinuities/normal faults dipping 60° to the South-West, with a 150-m average spacing. These structures form the landslide main and secondary scarps (Jomard 2006).
– a N010-30°E set of discontinuities/strike-slip dipping 70° to 80° to the South-East and the North-West, sometimes containing a thick filling of tectonic breccia. These structures limit the extension of the landslide to the North-East and the South-West.

The active landslide body can be schematically divided into three zones according to the rock fracturing and the spatial distribution of surface displacement rates (Cappa et al. 2004):

1. The main unit separated in two parts by a major scarp, is located at an elevation between 1100 and 1600 m (Fig. 1b, c). The scarp is oriented N 090° E and is dipping 50° towards the valley. These two parts consist of fractured rocks moving downslope at a velocity varying from 45 to 90 cm year^{-1} (Fig. 2)
2. The upper North-East unit (Fig. 1b, c) which behaves as an isolated block sliding along its own failure surface and overlapping the main central unit at a velocity varying from 100 and 380 cm year^{-1} (Fig. 2)
(3) The upper North-West unit (Fig. 1b, c) which behaves as a fractured rock mass with active tension cracks and moves at a velocity varying from 20 to 70 cm year^{-1} (Fig. 2)

Recent evolution of the landslide kinematics

The onset of the La Clapière movement is dated around the years 1950–1955 (even if a main scarp was already visible in 1937; Follacci 1987), possibly as a consequence of the major flood events of the Tinée river in 1951–1957 and a destabilization of the lower parts of the slope (Guglielmi et al. 2005). For the period 1951–1983, the landslide velocity is estimated from the correlation of aerial orthophotographs acquired in 1951, 1964, 1974 and 1983 (e.g. mean velocity values in green in Fig. 2). The velocity increased from 50 cm year^{-1} for the period 1951–1966 period to 150 cm year^{-1} for the period 1974–1983 (Follacci et al. 1988).

Since 1982, the landslide surface displacements are monitored by total station on a series of 43 targets (Fig. 2) at a monthly frequency (Follacci et al. 1988; 1993). According to Follacci (1987), the parallelism of the directions of motion of the benchmarks and the synchronism of the seasonal accelerations support the hypothesis of a deep failure. The grey line (Fig. 2) represents the monthly velocity of benchmark 10 which is located in the central part of the landslide and which can be considered as representative of the landslide kinematics for the period 1982–1995 (Helmstetter et al. 2004). An increase of this benchmark velocity occurs between January 1986 and January 1988, up to 8 cm day^{-1} during summer 1987 and 9 cm day^{-1} in October 1987. From 2000, the monthly velocity is calculated for ten targets (five historical targets numbered 6, 10, 16, 17, 24 and five new targets numbered 32, 34, 44, 43, 54; Fig. 2). For this period, the velocity varies from 1 cm day^{-1} (ca. 3.5 m year^{-1}) in 2000 to 2.5 cm day^{-1} (9 m year^{-1}) in 2001 which is the maximal annual velocity recorded (Fig. 2b). From 2002 to 2007, the landslide velocity decreases to less than 0.2 cm day^{-1}. In spring, a small acceleration phase is observed before the stop of the total station measurements in June 2009. No ground-based surface displacement observations are available for the period 2009–2011. In 2011, GPS receivers were installed on the landslide at location CLP1 and CLP2 (Fig. 2). The French National Landslide Observatory (OMIV) is now in charge of the continuous monitoring of the landslide. A short acceleration has been observed in the spring of 2013 (ca. 1 cm day^{-1}) but not comparable to those of 1987 and 2001.
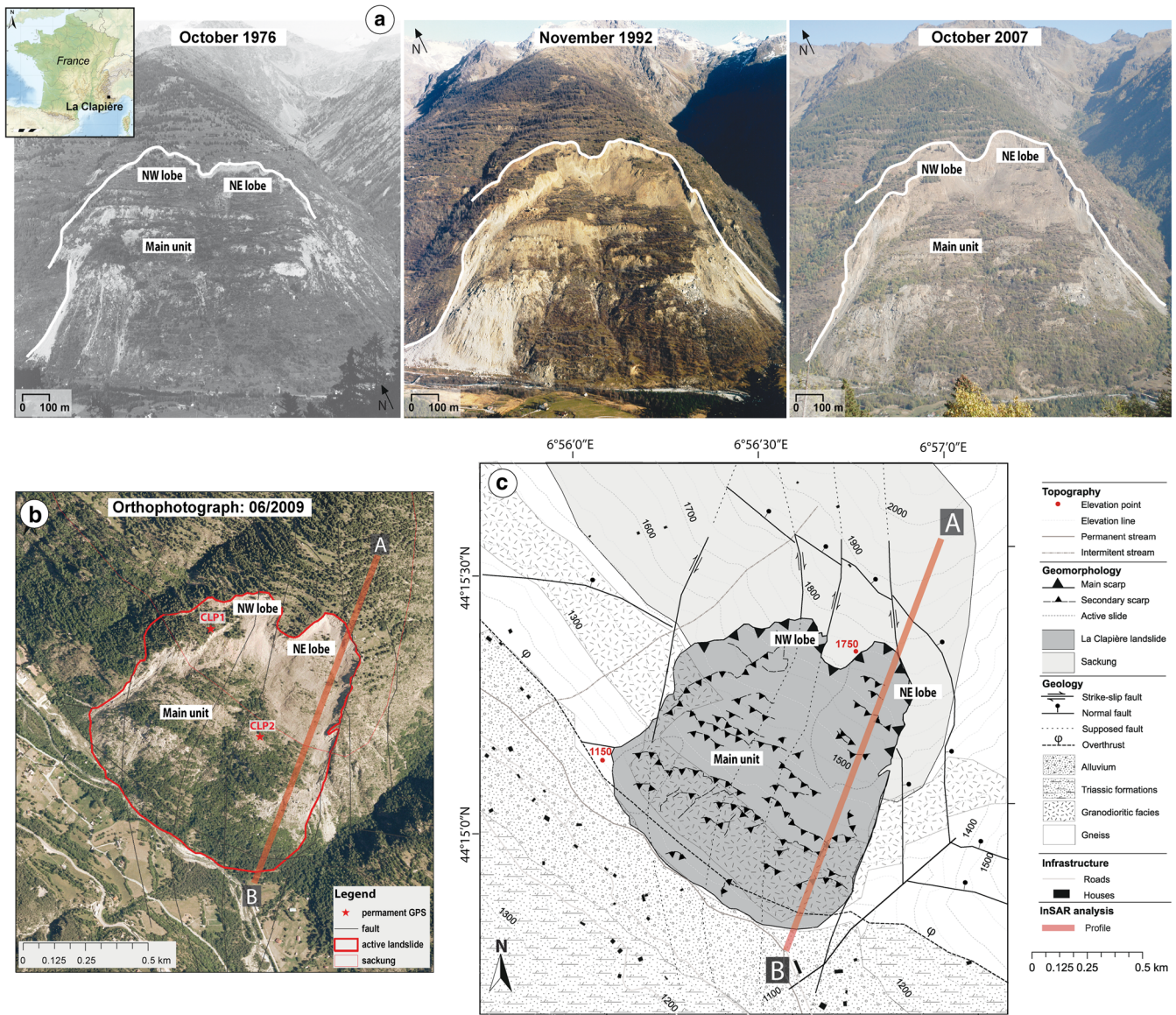
Fig. 1 Geomorphology of the La Clapière landslide. **a** Photographs of the La Clapière landslide in 1976, 1992 and 2007. **b** Orthophotograph of the landslide in 2009. **c** Morpho-structural map of the landslide.

Methods

Dataset: SAR images and ground-based total station measurements

The dataset (Fig. 3) consists of satellite SAR images, airborne orthophotographs, a high resolution digital surface models (DSMs) and displacement measurements from a ground-based total station. We use 15 ALOS/PALSAR images (processed at Level 1.0) acquired from March 2007 to July 2010 (Fig. 3). This large wavelength L-band radar sensor ($\lambda=23.8$ cm) is more suitable for landslide monitoring than shorter C-band and X-band radar sensors as it allows higher quality of the backscattered phase signal on rapidly evolving ground surfaces (vegetation, soil surface state, micromorphology and roughness; Wei and Sandwell 2010).

The ALOS/PALSAR catalogue consists of SAR images acquired along ascending orbit (track 880) and with a high-resolution Fine Beam Polarization (FBS) mode. For all images, the pixel dimensions are 9.78 m and 7 m along the azimuth and range direction, respectively. The mean look angle θ is 38.7° over the scene, and the off-nadir azimuth α_d is 75.8°. For the InSAR processing, the criteria used to select the image pairs are as follows: (1) a perpendicular baseline ($B_\perp$) smaller than 1000 m; (2) a temporal baseline (B_T) between both images of 46 days; and (3) a net rainfall amount of less than 200 mm between consecutive dates (Fig. 3). To avoid decorrelation due to the presence of snow cover, we also excluded scenes acquired in winter. The four interferograms analyzed in this work are named T1, T2, T3 and T4 (Fig. 3).

A medium resolution (25 m) DSM from the French National Mapping Agency (BD ALTI®, IGN), resampled at 0.000088° (9.78 m) and projected in geographic-WGS84 coordinates was used for the InSAR processing. A high resolution (0.000052°) airborne LiDAR DSM, resampled at a pixel size of 5 m, is used for calculation of the ground displacements. Three aerial
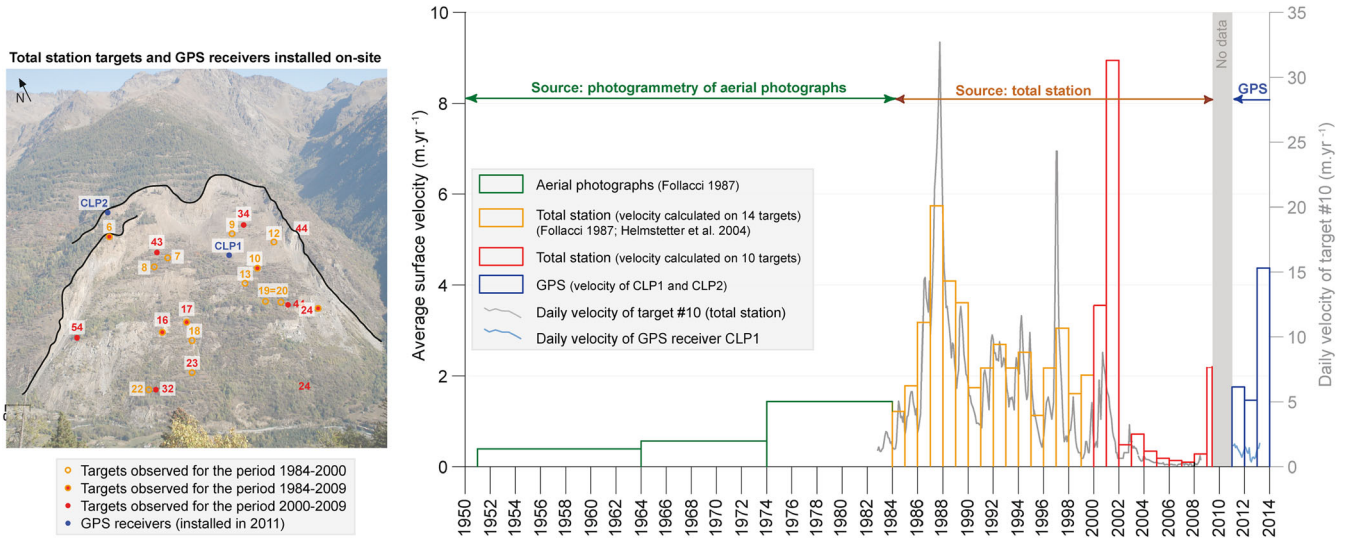
Fig. 2 Evolution of the mean velocity of the landslide body from 1950 to 2013 measured by photogrammetry of airborne photographs (1951–1984), by ground-based total station measurements on benchmarks (1984–2009) and by continuous GPS measurements (2011–2013). The velocity time series is constructed from previous studies (Follacci 1987; Helmstetter et al. 2004) and calculated from total station observations provided by the Centre d'Etudes Techniques de l'Equipement (CETE-06).

orthophotographs (0.5 m) of 2004, 2009 and 2012 were used for the morphological analysis and the interpretation of the results.

Total station measurements were provided by the public authority Centre d'Etudes et d'Expertise sur les Risques, l'Environnement, la Mobilité et l'Aménagement (CEREMA in charge of the slope risk management). The automated total station measures distances and horizontal/vertical angles on 1 to 2-km distant targets in line-of-sight. Two to five of the targets used for total station measurements were acquired daily over the period 2000–2009.

D-InSAR processing and interpretation
The processing of the SAR images and interpretation methodology of the interferograms are summarized in Fig. 4. Each

interferogram consists of the calculation of phase differences ($\Delta\Phi_{int}$) between two co-registered SAR images (Eq. 1):

$$\Delta\Phi_{int} = \Phi(t_0) - \Phi(t_1) + \Delta\Phi_{def} + \Delta\Phi_{orb} + \Delta\Phi_{topo} + \Delta\Phi_{atm} + \Delta\Phi_{noise} \quad (1)$$

where $\Delta\Phi_{int}$ is the SAR interferometric phase, $\Delta\Phi(t_0)$ and $\Delta\Phi(t_1)$ are the SAR phase values at, respectively, day t_0 (reference) and day t_1, $\Delta\Phi_{def}$ is ground deformation (between two acquisition times), $\Delta\Phi_{orb}$ is orbital contribution (due to changes of the satellite orbital geometry), $\Delta\Phi_{topo}$ is topographic contribution, $\Delta\Phi_{atm}$ is atmospheric contribution (due to difference of signal propagation in the atmosphere) and $\Delta\Phi_{noise}$ is noise contribution (corresponding to changes in the scattering properties of the ground surface,
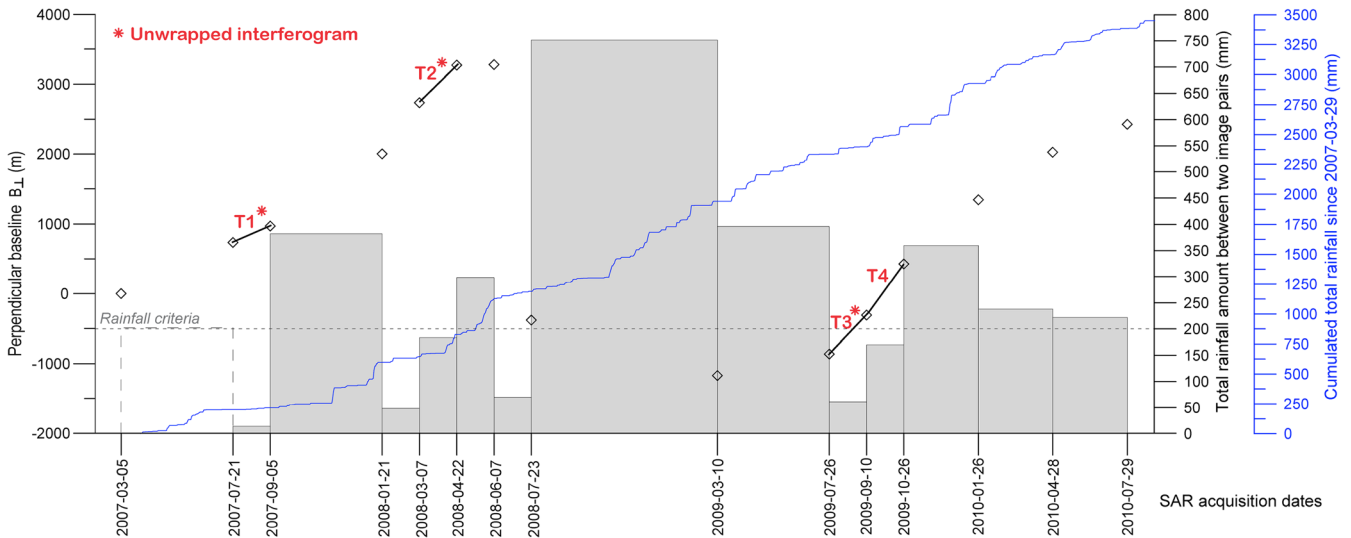
Fig. 3 Time acquisition and perpendicular baseline (*white point*) of the SAR images together with the cumulative net rainfall between consecutive SAR acquisitions (*grey box*) and for the complete time period (*blue line*) at the St-Etienne de Tinée meteorological station. The interferograms T1, T2, T3 (*unwrapped*) and T4 (*wrapped*) are indicated. A *dotted grey line* indicates the 200 mm of cumulated rainfall used as selection criterion for the SAR images
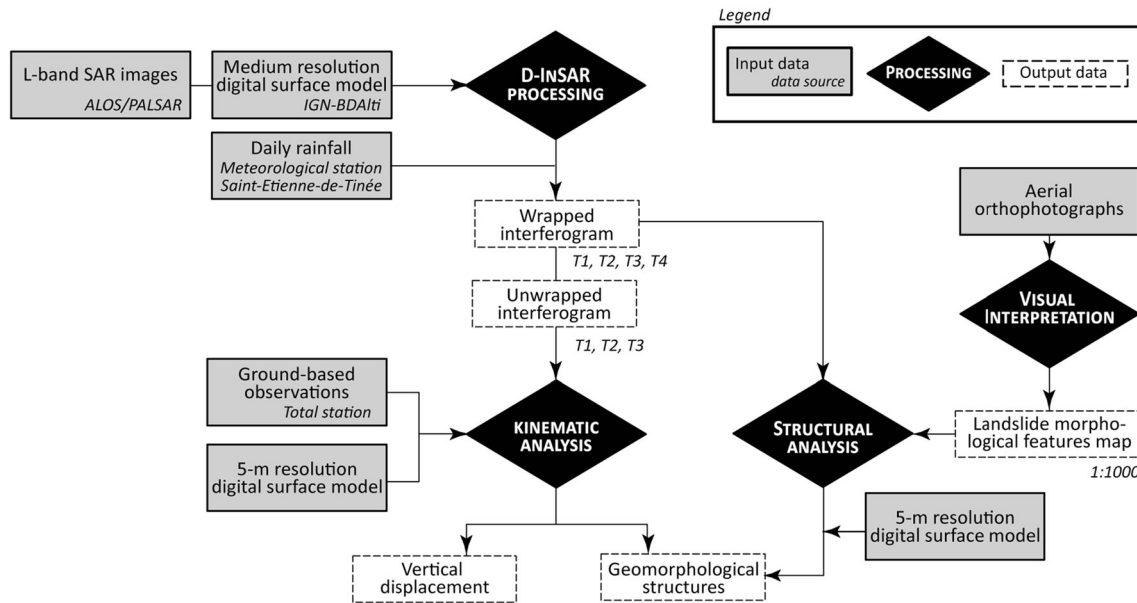
Fig. 4 Flowchart of the methodology and indications of the data and outputs used at each processing step (modified from Schlögel et al. 2015)

changes in the thermal properties of the atmosphere or ground surface or inaccurate image co-registration; Massonnet and Feigl 1998).

The co-registration between SAR images is performed using a quadratic fit with the software package NSBAS (Doin et al. 2011) to take into account orbital parameter and the topography. Then, the interferograms are processed with the software package ROI_PAC (Fig. 4; Rosen et al. 2004). The topographic contribution is corrected using the BDALTI® DSM (25 m) resampled at 10 m. The orbital contribution is corrected with precise satellite orbit data (<1 m) provided by the Japan Aerospace Exploration Agency (JAXA) fitted with a 2D linear offset ramp. Further, a range-dependent spectral filtering is applied to improve coherence of the interferograms with long spatial baselines with NSBAS.

After filtering, we interpret only the interferograms with coherence values higher than 0.30 (e.g. T1, T2, T3 and T4; Fig. 3). The phase values are unwrapped using the branch-cut unwrapping algorithm of Goldstein et al. (1988) and geocoded.

The interpretation of the interferograms is performed at the slope scale in a Geographical Information System (GIS). First, the interferograms are converted in the local reference system Lambert NTF Zone III and resampled at a pixel size of 9.78 m. The precise location and contours of the expected deformation area are mapped from the interpretation of the series of orthophotographs. Second, in order to compare the interferograms, we shifted the phase values taking as reference the portions of the terrain out of the landslide body. We subtracted the median phase values (Φ_{med}) of the area surrounding the landslide to the phase values of the sub-scene. The resulting phase values for the wrapped interferograms are thus expressed in the range $[-\pi-\Phi_{med}, \pi-\Phi_{med}]$.

The landslide morphological features (scarps, fractures, lobes, gullies) observed on the aerial orthophotographs and the DSM are used to guide the interpretation of the wrapped

and unwrapped phase values. For the analysis of the unwrapped phase values, we converted the phase values in displacement along the SAR LoS direction (D_{LoS}) using Eq. 2:

$$D_{LoS} = \lambda \Delta\Phi / 4\pi \qquad (2)$$

where λ is the wavelength, and Φ is the phase value.

Taking into account the spatial distribution of the phase values, we consider the portions of the terrain with absolute phase values $\Phi > 0.5$ (corresponding to a LoS displacement of 0.9 cm) as 'moving' areas. According to Schlögel et al. (2015), various phase values and displacement fields can be observed at the scale of a landslide due to heterogeneous local movements:

- In the lower part of the landslide, the horizontal component of the displacement (expressed along the downslope direction) is dominant with an accumulation of the displaced material; this movement corresponds to negative phase values ($\Phi < -0.5$).
- In the upper part of the landslide, close to the main and secondary scarps, the vertical component of the displacement is dominant with a subsidence and a transport of material downslope; this movement corresponds to positive phase values ($\Phi > 0.5$).

Using ground-based monitoring data, we assumed a main displacement direction for all the kinematical units of the landslides. Two cases are considered. The first case corresponds to a vertical motion associated with a depletion of material (preferentially located in the upper part of the landslide) or with an accumulation of material (preferentially at the toe of the landslide). Therefore, we convert the LoS

displacement into ground vertical displacement (D_{vert}) with Eq. 3:

$$D_{vert} = D_{LoS}/(n_z.n_{LoS}) = -D_{LoS}/\cos\theta \qquad (3)$$

where n_z is the vertical unit vector (positive upward), n_{LoS} is the unit vector in the LoS direction and θ is the mean incidence angle (equal to 39.7° in this region). A positive vertical displacement ($D_{vert} \geq 0$) corresponds to a subsidence; a negative vertical displacement ($D_{vert} \leq 0$) corresponds to an uplift or an accumulation of material.

The second case corresponds to an along-slope motion, observed in the case of a predominant translational sliding. According to the orientation of the displacement field of the landslide (ca. N210°E) and the mean slope gradient (ca. 33°) close to the incidence angle (θ), we decided to project the displacement only in the vertical direction. SAR images acquired in ascending orbits would have been a source of information to calculate the 'along-slope' displacement vectors, but unfortunately, no images are available in the satellite archives.

Results: analysis of the landslide kinematics

The landslide kinematics was analyzed for the period 2007–2010 in terms of the spatial distribution of velocity and the evolution of velocity over time by combining the ground-based total station measurements and the InSAR-derived displacement fields.

Landslide velocity fields from the ground-based total station measurements

The total station installed in front of the landslide is the only source of ground-based surface displacement measurements for the period 2000–2009 (Fig. 5a). Trends in the surface displacements can be identified for a series of six targets located along a cross section from the scarp to the toe of the landslide. According to their position within the landslide body, the targets have different kinematic behaviour. The target #40 located at the crown is stable; in the landslide body, the displacements are higher for the targets #34 and #10 located in the upper part than for the targets #44 and #24 located in the middle and lower parts. The cumulated displacements are in a range of factor 5 for the period 2000–2009, from 10 m at the toe (#24) to nearly 50 m at the base of the main scarp (#34).

Figure 5b also highlights the important acceleration observed in 2000–2001. The acceleration started at different times according to the landslide units, in June 2000 for target #34 at the base of the scarp to December 2000 for the targets #44 and #24 in the lower parts. The peaks of velocity are observed from April to August 2001; the deceleration occurred in November 2001. A small rise in velocity is again observed for all targets between November 2002 and July 2003. Then, for almost 5 years, the landslide exhibits constant velocity for all units. The onset of a new acceleration is observed in February 2009 at targets #6, #44 and #34. Unfortunately, the total station measurements have ceased in July 2009 due to malfunctioning of the instrument and expensive maintenance costs.

The evolution of the displacements per component (E, N, Z) is presented in Fig. 6. The daily position of the targets at midday (12.00) and the error bars are plotted for four targets for the period 2007 to 2009.

The variability of measurements is more important for the targets located in the upper part of the landslide where the distances total station-target are longer. Considering this variability, we still consider the target #40 as stable even if a tilt is observed (with the succession of positive and negative variations) due to its position at the crown. In the upper part of the landslide body, the benchmark #34 is the most rapid, especially in the North component; from April 2008, the velocity increases from 0.1 to 1.6 cm day^{-1}. Best-fit (R^2 values>0.80) linear regression lines are
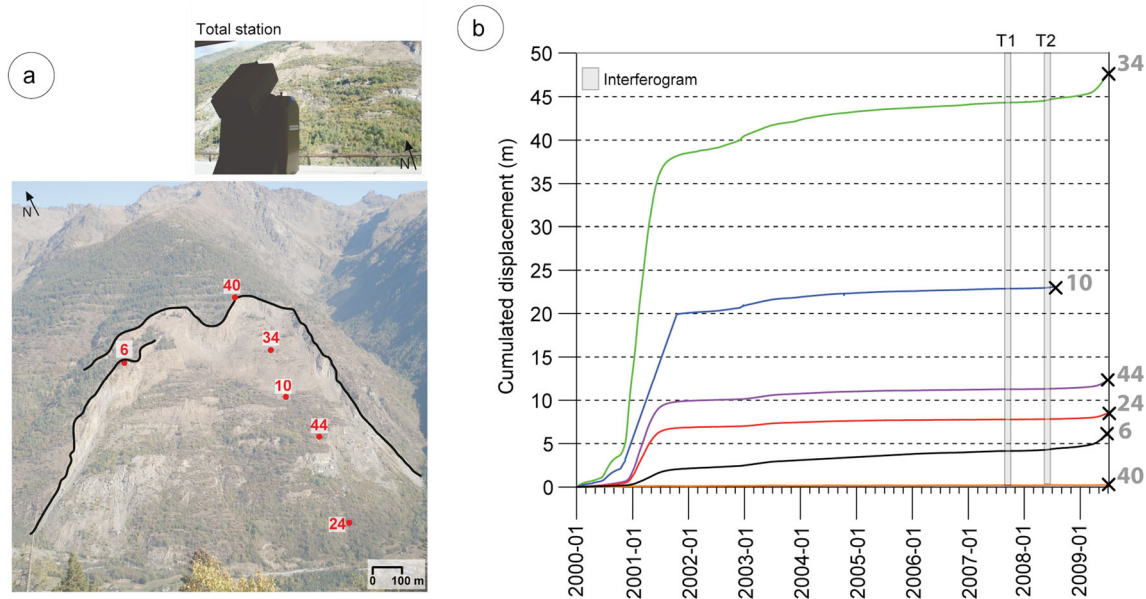
Fig. 5 Landslide surface displacement measured by total station on a series of targets. **a** Photograph of the total station and location of the targets used in the analysis. The targets are located along a cross section in the South part of the landslide. **b** Evolution of the distance tacheometer-target for six benchmarks from 2000 to 2009. The black cross indicates the stop of the measurement. The *grey lines* indicate the interferograms available during the monitoring period (T1, T2)
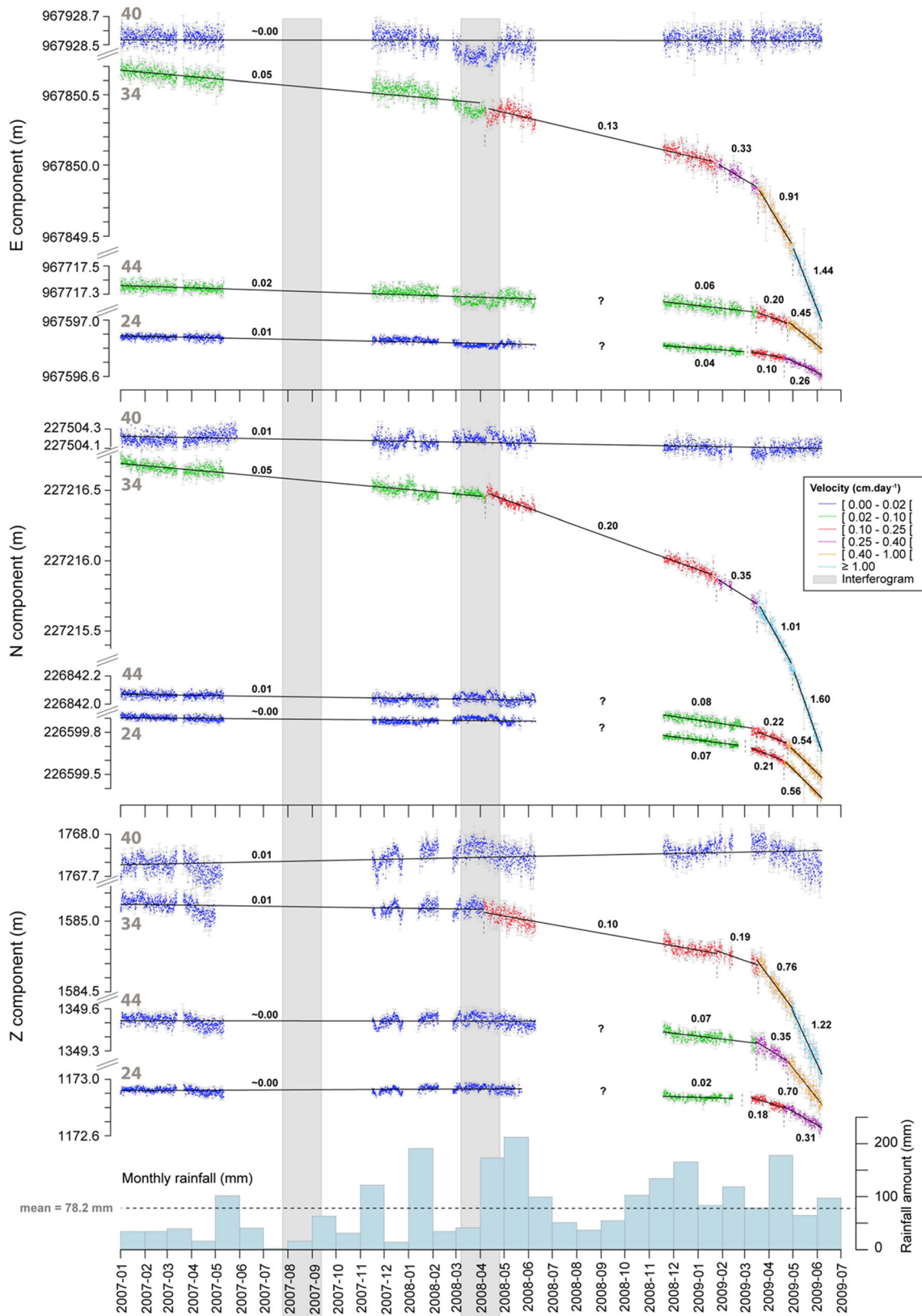
Fig. 6 Evolution of the E, N and Z components of four targets for the period 2007–2009. The velocity is calculated by fitting a regression line per sub-periods of velocity assumed constant and to a R^2 values higher than 0.80. The value of the velocity (in cm day^{-1}) is indicated above the regression line. Six classes of velocity are identified. The monthly rainfall is indicated for the monitoring period; the average monthly cumulated rainfall is 78.2 mm for the period

plotted on the displacement time series to estimate the velocity (Fig. 6).

In the lower parts, the velocity decreases and the type of deformation changes; the maximal velocity is observed for target #44 with a value of 0.7 cm day^{-1} in the Z component. The target #24 presents lower velocity than the target #44 but the trend is similar; the maximal velocity reaches 0.5 cm day^{-1} in the N component and only 0.3 cm day^{-1} in the Z component.

The analysis of the target displacements indicates that the acceleration of the landslide does not occur at the same time for all targets and that the periods of high velocity do not have the same duration. It suggests that the geological structures of the landslide control the spatial distribution of velocity and that the North-East lobe has a completely different kinematic behaviour.

On the basis of the analysis, two kinematic regimes are identified for the years 2007–2009 consisting in periods of slow displacement (velocity <0.2 cm day^{-1}) and periods of high displacement (velocity >0.2 cm day^{-1}). Figure 8 presents the geometry of the 3D vectors for the same targets for respectively the slow-moving period (Fig. 7a) and the fast-moving period (Fig. 7b). The ratios of horizontal (E-N) to vertical (Z) displacements are presented for each target respectively in blue (slow-moving period) and red (fast-moving period) colours. For the slow-moving period (Fig. 8a), the horizontal displacements are generally larger than the than vertical displacement testifying of a predominant translational sliding of the slope. For the fast-moving period (Fig. 7b), larger vertical displacements are observed

than for the slow-moving period indicating that the deformation combines translational and rotational sliding. The directions of the displacement are also analyzed in relation to the local topographic slope gradient computed on a 5-m resolution digital surface model. Figure 7 indicates that the displacement vector is generally parallel to the local slope gradient for the period of low velocity (Fig. 7a) while it is oriented downward of the local slope gradient for the period of high velocity (Fig. 7b).

Landslide deformation fields from InSAR

Figure 8 presents the interferograms T1, T3 and T4. Areas with coherence below the threshold of 0.3 are in grey. At T1, the active area is limited to the lower part of the landslide while ground displacements outside of the landslide, east of its upper geomorphological boundary occur. The landslide can be divided in three units delimited by yellow-orange colours at the top, blue-purple colours at the toe and green colours at the Northern part of the lateral scarp. The distribution of phase values is oriented NW-SE, i.e. perpendicular to the slope direction and parallel to the main and secondary scarps. The North-East lobe is clearly identified along the main scarp. The deformation fields for these three 46-day periods (T1, T2, T4) can be explained by high velocities and depict the geometry of the multiple rotational slides (secondary scarps and counter slopes) observed in the upper part of the landslide.

Figure 9 presents the unwrapped phase values in the three interferograms. Phase unwrapping is complex within the landslide contours due to important changes of the ground properties.
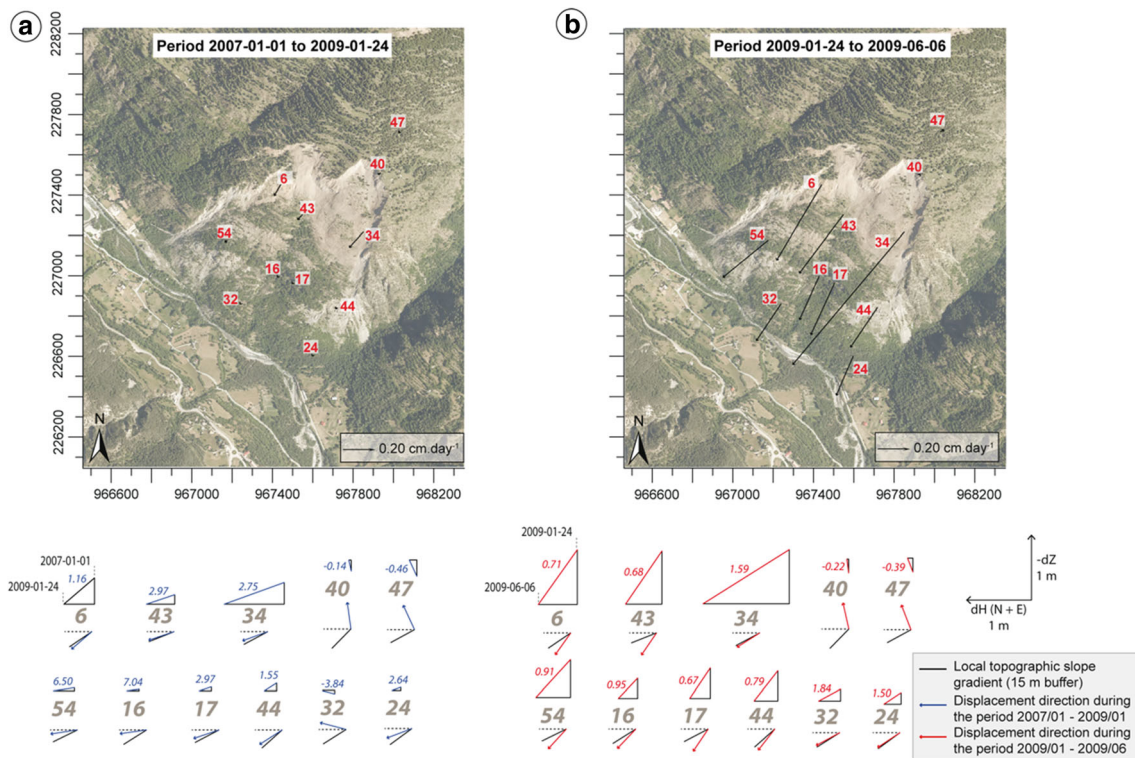
Fig. 7 Analysis of the geometry of the 3D displacement vectors for a period of low velocity (<0.2 cm day^{-1}; <2009/01/24) and a period of high velocity (>0.2 cm day^{-1}; >2009/01/24). **a** Map of 3D vectors for several targets for a period of low velocity. The ratio of vertical to horizontal displacement is indicated in *blue* for the period from 2007/01/01 to 2009/01/24. **b** Map of 3D vectors for several targets for a period of high velocity. The ratio of vertical to horizontal displacement is indicated in *red* for the period from 2009/01/24 to 2009/06/06. The horizontal displacement corresponds to the sum of the North (N) and East (E) components. The directions of displacement are compared to the local slope gradient
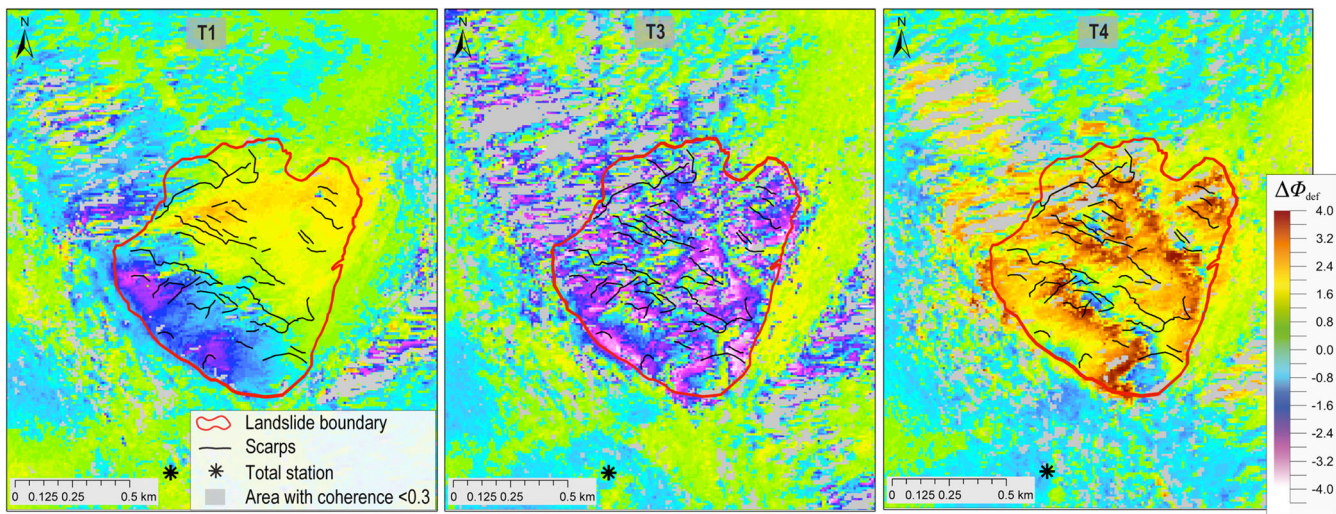
Fig. 8 Wrapped interferograms for the periods T1, T3 and T4. The phase values in the assumed stable areas outside of the landslide limits have been shifted to zero. The landslide boundary is indicated in *red* and the scarps are plotted in *black*. Areas of the interferograms with coherence value lower than 0.3 are in *grey*

Unwrapping was particularly difficult for the interferogram T3 probably due to higher velocities.

In the upper part, we observe positive D_{LoS} values on the interferograms T1, T2 and T3 corresponding to a ground LoS displacement away from the satellite, consistent with the subsidence of material in the ablation zone due to sliding of material at depth. In the lower part, we observe negative D_{LoS} values on the three interferograms corresponding to a ground LoS displacement towards the satellite consistent with the uplift at the toe due to material accumulation at depth. This non-uniform displacement gradient from the top to the bottom of the landslide is identified for the three interferograms.

The amplitude of the vertical displacements varies in time (Fig. 9). The maximum absolute D_{LoS} values reach respectively 4.6±0.9 cm for T1, 12.6±0.9 cm for T2 and 11.4±0.9 cm for T3, corresponding to vertical displacements of 6.0±1.1 cm (T1), 16.4 ±1.1 cm (T2) and 14.8±1.1 cm (T3). For T4, statistics are not computed because phase unwrapping was only possible on a very limited portion of the landslide (less than 10 % in surface) due to decorrelation and probably high displacement gradients. These observations indicate that the displacements are not steady-state with significant variations in space and time.

Spatial variations in D_{LoS} and V_{LoS} values along the profile A–B (Fig. 10) allow distinguishing several kinematic units. Three kinematic units, limited by morphological structures, are identified from the unwrapped phase values, in agreement with the wrapped phase field in Fig. 8, and displacement observed in the vertical and horizontal components by total station measurements (Fig. 7), the multiple rotational slides observed by Jomard et al. (2007), and the inferred geometry of the slip surface of Cappa et al. (2004).

Discussion

The space and time variations of the 3D displacement field is interpreted in relation to the geological structure of the slope, the geometry of the slip surface and geomorphological features at the surface with the presence of several scarps and counterslopes at the top and accumulation lobes at the bottom (Fig. 10). On average, the vertical velocities are in the range −0.05 and −0.10 cm day^{-1} in the upper part of the slope, decrease to less than −0.05 cm day^{-1} in the middle part of the slope and to 0.02 to 0.05 cm day^{-1} in the lower part of the slope. The movement, interpreted from both ground-based and satellite InSAR observations, corresponds mainly to subsidence at the top, to translation (along the slope of the slip surface) in the middle part and to uplift at the bottom (Fig. 10). From the elevations 1300 to 1750 m, the landslide material is characterized by extensional features; from the elevations 1225 m to 1300 m, the landslide material is characterized by compressional features.

For the period 2007–2009, an increase in landslide velocity is observed for all units, even though the quantification if this acceleration is difficult as phase unwrapping was not possible throughout the whole landslide for the three interferograms. In the subsiding area, the vertical velocities V_{vert} are in the range 0.25 to 0.30 cm day^{-1} at T3 while the maximal vertical velocities are in the range from 0.10 to 0.15 cm day^{-1} at T2 and T1. In the accumulation area at the toe, the vertical velocities are in the range from 0.05 to 0.10 cm day^{-1} for T1, T2 and T3, though locally a slightly higher at T2 (>0.10 cm day^{-1}) according to the values along this profile.

The spatial pattern of the velocity field in the period 2007–2009 is similar to the pattern measured by Girault and Terrier (1994) by terrestrial photogrammetry for the period 1970–1989, with mainly accumulation of material at the toe (expressed by a progression of material downslope) and a subsidence movement at the top (expressed by a retrogression of material upslope in the horizontal component; Fig. 11b). Elevation of the boundary between subsidence and accumulation is estimated at 1375 m in 1989 (Girault and Terrier, 1994) while it is located at 1300 m in 2009 (Fig. 10). The vertical velocities measured by InSAR are lower for the period 2007–2009 than for the year 1991 when vertical velocities in the range from 0.20 to 0.70 cm day^{-1} were measured from the analysis of C-band ERS interferograms (Fruneau et al., 1996).
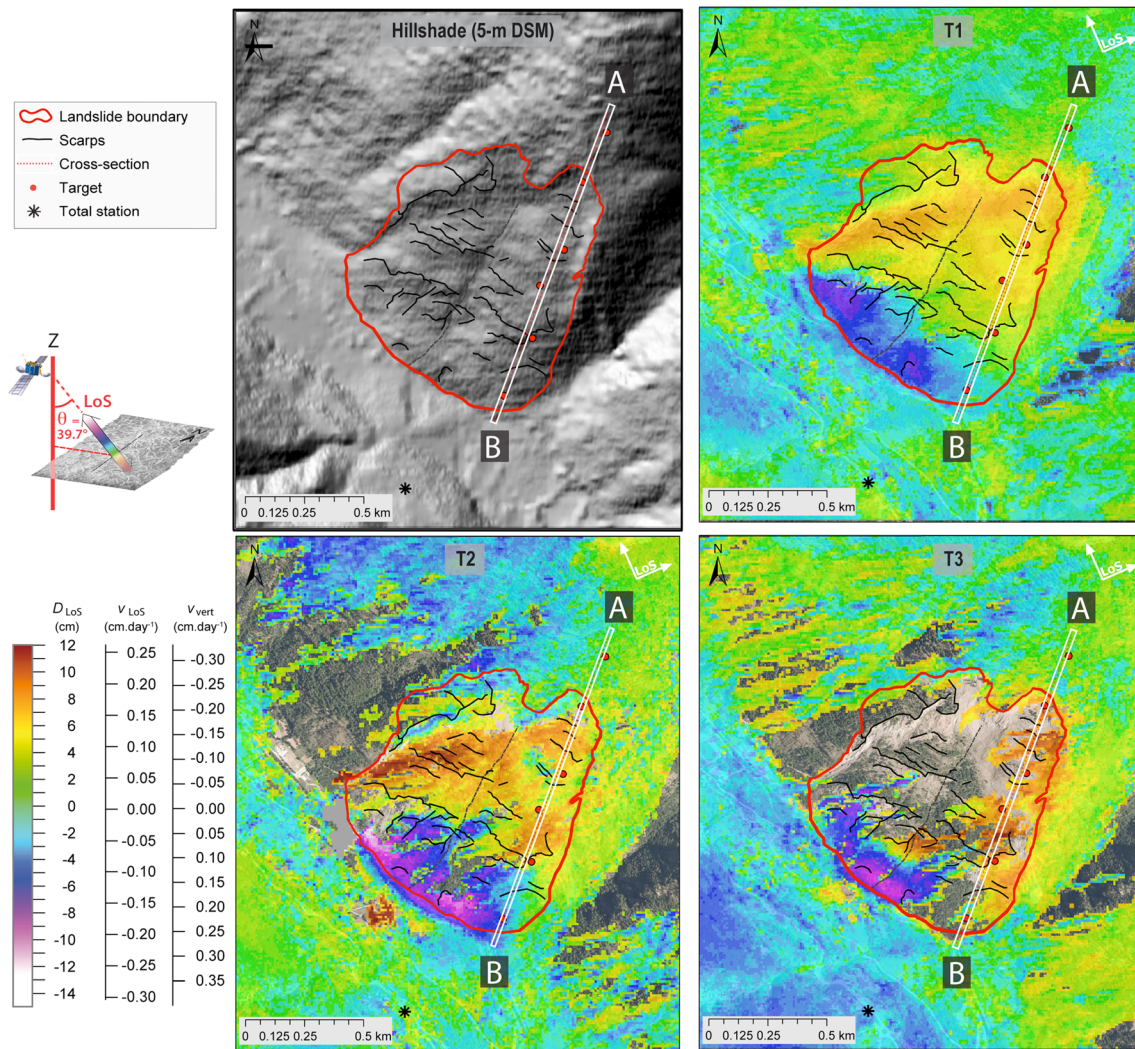
Fig. 9 Displacement (cm) and velocity (cm day^{-1}) fields observed for the La Clapière landslide. The hillshade of a 5 m resolution digital surface model (year 2009) and the unwrapped interferograms for the periods T1, T2 and T3 are presented

For the period 2007–2009, higher surface velocities are observed for the period T3 in relation with larger amounts of net and effective (precipitation minus evapotranspiration) cumulated rainfall over 120 days (Fig. 12). The evapotranspiration rate is calculated with the Penman-Monteith method. The effective cumulative rainfall amounts for the 40 days before the first SAR image acquisition are higher for T3 (~100 mm) than for T1 (~30 mm) and T2 (~50 mm) but are lower for T3 if we consider only the 25 days before the SAR acquisition of July 26th 2009. This means that short and intense meteorological events are not linked to the acceleration observed for the period T3. In addition, the 30-year-long averaged net rainfall values for the 4 months before July 26th (averaged for the past 30 years) is lower than the 4-month-long observed net rainfall for the year 2009. Thickness and duration of snow cover (2.1 m at 2100 m elevation and 129 days, respectively) were larger during the winter 2008–2009, than during the winter 2007–2008 (1.4 m at 2100 m elevation; 109 days). According to Cappa et al. (2004) and Lebourg et al. (2005), in case

of abnormal rainfall events (up to 200 mm) and/or rapid snowmelt in a localized range of elevations (1800–2500 m), the water can percolate quickly within the landslide body through the network of fractures and faults and induce an acceleration of the landslide motion.

Conclusion

This work demonstrates the potential of L-band ALOS/PALSAR archive images to estimate the displacement field of large and rapid landslides with a traditional D-InSAR approach. For such case studies, the longer wavelength of L-band SAR sensors are suitable to preserve high spatial and temporal correlations and to quantify the movement of the ground affected by large changes in soil surface properties.

Even with complex field conditions (e.g. slope gradient and orientation of the landslide vs. ascending track of the satellite), an analysis of the landslide kinematics over the period 2007–2009 is proposed. The analysis of the wrapped phase values and in
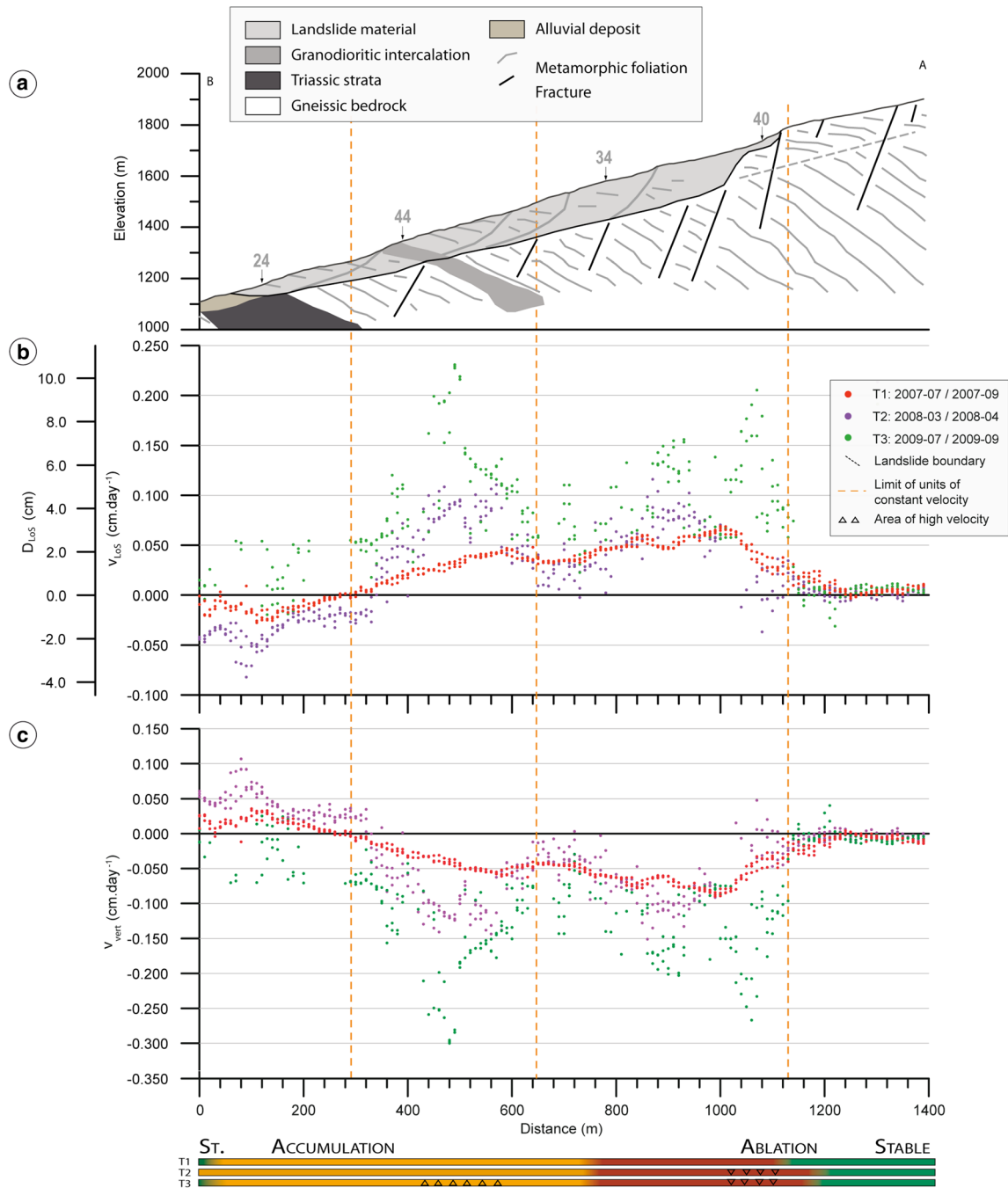
Fig. 10 Displacement (DLoS, DVert; cm), velocity (VLoS; cm day^{-1}) observed at the La Clapière landslide from L-band ALOS/PALSAR SAR data. **a** Topography, lithology and geometry of the slip surfaces along a longitudinal cross section in the Eastern part of the landslide (*A–B*). The location of the 30-m-width profile is indicated in Fig. 9, and the landslide geometry is from Cappa et al. (2004). The displacement pattern is indicated by the theoretical vectors for each unit. **b** LOS displacements (DLoS) and velocity along profile *A–B* for the unwrapped interferograms T1, T2 and T3. **c** Vertical velocity (Vvert) along profile *A–B* for the unwrapped interferograms T1, T2 and T3. The *colour bars* indicate changes in the movement type (subsidence in *red*, accumulation in *orange*, stable slopes in *green*)

particular the high large gradients allows detecting the active geological structures (fractures, faults) and morphological structures (scarps, grabens, gullies, steep slopes) and their role on the dynamics of the slope. The analysis indicates that the direction of the motion is (1) perpendicular to the N 140° E overthrust and to the main fractures of the massif and (2) parallel to the N010-030°E-

oriented faults crossing the landslide. Several sliding units were identified from the displacement field derived from InSAR and ground-based measurements.

The analysis of the unwrapped phase values (for portions of the slope where unwrapping was possible) indicates an acceleration of the upper part of the landslide with vertical velocities V_{vert} ranging
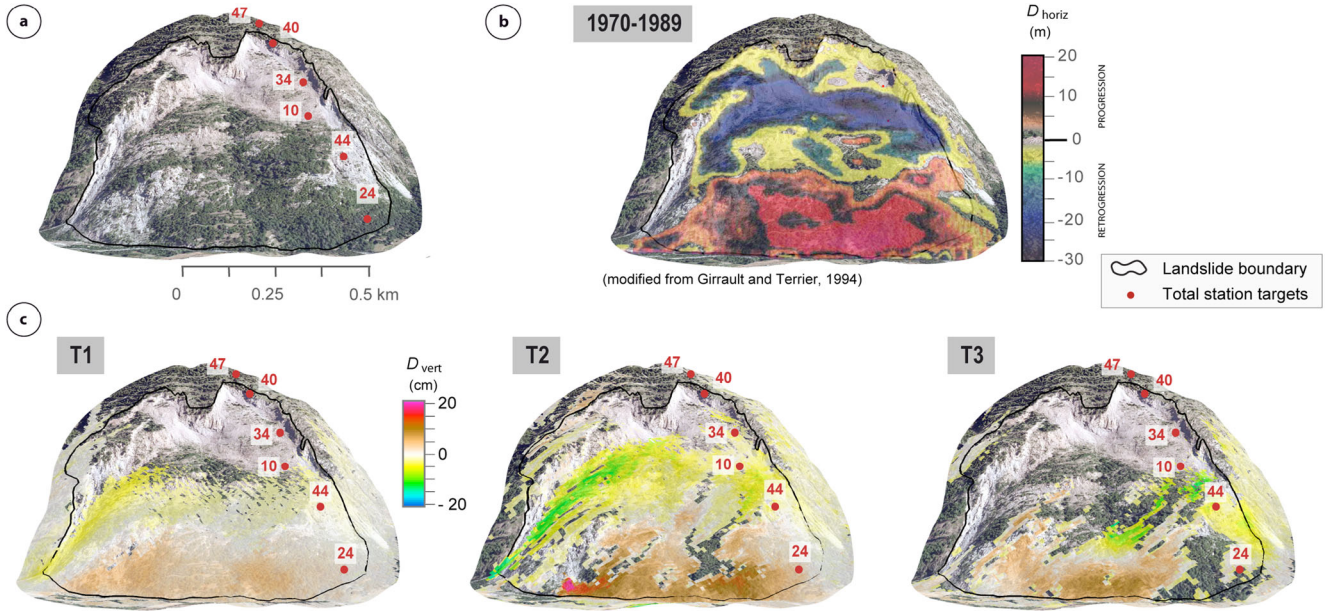
Fig. 11 Horizontal and vertical displacement fields of the La Clapière landslide. **a** Orthophotograph of the landslide in 2009. **b** Mean horizontal displacement field (dH) measured by comparison of digital surface models (DSM) between 1970 and 1989 (modified from Girault and Terrier 1994). **c** Vertical displacement field (dV) measured by InSAR at T1, T2 and T3. The landslide boundary is indicated in *black* and the targets by *red dots*

from 0.1 cm day^{-1} in 2007 to 0.15 cm day^{-1} in 2008 and to 0.25–0.30 cm day^{-1} in 2009. This acceleration identified in 2009 with InSAR is also observed on ground-based measurements. The deformation field is complex and controlled by the main structural discontinuities crossing the landslide, such as intermediate scarps in the upper part and the Barre d'Iglière in the lower part. The triggering factors of the 2009 acceleration are difficult to highlight. The combination of a thicker snow cover, a higher number of days with a snow cover and a net rainfall amount cumulated over 120 days higher than the 30-year-long averages may explain the acceleration.

ALOS/PALSAR imagery, even if only a limited archive data is available, allows complementing information from other satellite SAR sensors to construct time series of surface deformation and document the complex destabilization of the La Clapière slope. The estimated displacement rates are in the range of the ground-based total station observations and consistent with other monitoring studies.
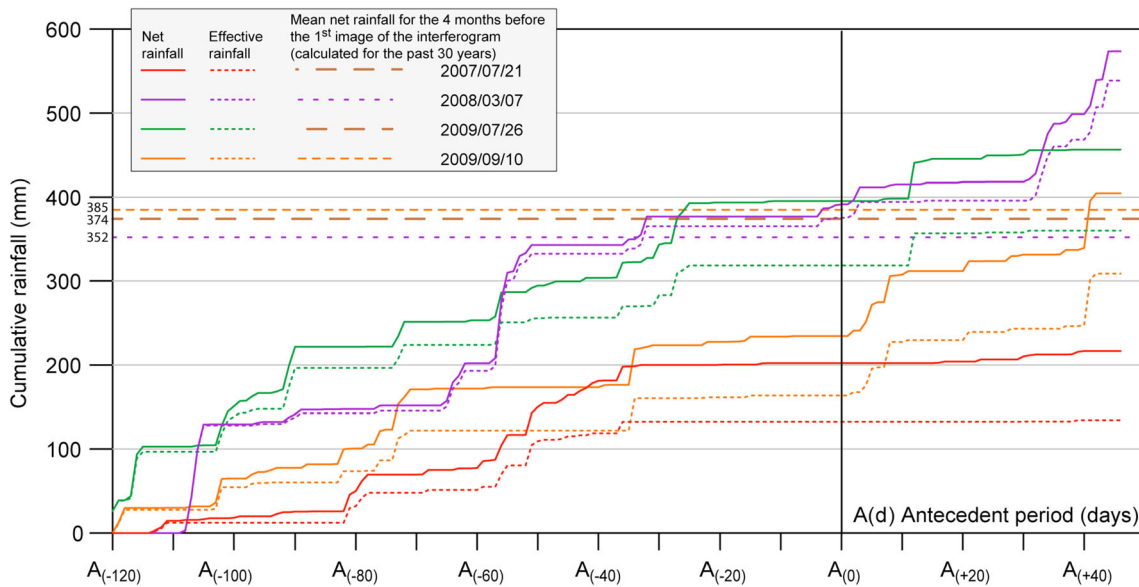
Fig. 12 Landslide movement in relation with rainfall amounts over several time spans. Antecedent net and effective (precipitation minus evapotranspiration) cumulative rainfall at the Saint-Etienne-de-Tinée rain gauge from 120 days before the first SAR image acquisition (i.e. A(0)) and for temporal baseline of 46 days (T1, T2, T3, T4). Thirty-year-long averaged net rainfall values for the 4 months before the first acquisition are indicated by *coloured dotted lines*

References

Agliardi F, Crosta G, Zanchi A (2001) Structural constraints on deep-seated slope deformation kinematics. Eng Geol 59:83–102

Berardino P, Fornaro G, Lanari R, Member S, Sansosti E (2002) A new algorithm for surface deformation monitoring based on small baseline differential SAR interferograms. IEEE Trans Geosci Remote Sens 40:2375–2383

Berger M, Moreno J, Johannessen JA, Levelt PF, Hanssen RF (2012) ESA's sentinel missions in support of Earth system science. Remote Sens Environ 120:84–90

Bois T, Bouissou S, Guglielmi Y (2008) Influence of major inherited faults zones on gravitational slope deformation: a two-dimensional physical modelling of the La Clapière area (Southern French Alps). Earth Planet Sci Lett 272:709–719

Booth AM, Lamb MP, Avouac J-P, Delacourt C (2013) Landslide velocity, thickness, and rheology from remote sensing: La Clapière landslide, France. Geophys Res Lett 40:4299–4304

Cappa F, Guglielmi Y, Soukatchoff V, Mudry J, Bertrand C, Charmoille A (2004) Hydromechanical modeling of a large moving rock slope inferred from slope levelling coupled to spring long-term hydrochemical monitoring: example of the La Clapière landslide (Southern Alps, France). J Hydrol 291:67–90

Cascini L, Fornaro G, Peduto D (2009) Analysis at medium scale of low-resolution DInSAR data in slow-moving landslide-affected areas. ISPRS J Photogramm Remote Sens 64:598–611

Casson B, Delacourt C, Allemand P (2005) Contribution of multi-temporal sensing images to characterize landslide slip surface—application to the La Clapière landslide (France). Nat Hazards Earth Syst Sci 5:425–437

Colesanti C, Wasowski J (2006) Investigating landslides with space-borne synthetic aperture radar (SAR) interferometry. Eng Geol 88:173–199

Corsini M, Ruffet G, Caby R (1994) Alpine and late Hercynian geomorphologic constraints in the Argentera Massif (Western Alps). Eclogae Geol Helv 97:3–15

Delacourt C, Allemand P, Casson B, Vadon H (2004) Velocity field of the "La Clapière" landslide measured by the correlation of aerial and QuickBird satellite images. Geophys Res Lett 31:1–5

Delacourt C, Allemand P, Berthier E, Raucoules D, Casson B, Grandjean P, Pambrun C, Varel E (2007) Remote-sensing techniques for analysing landslide kinematics: a review. Bull Soc Geol Fr 178:89–100

Delteil J, Stephan J-F, Attal M (2003) Control of Permian and Triassic faults on Alpine basement deformation in the Argentera massif (external southern French Alps). Bull Soc Geol Fr 174:55–70

Doin M-P, Lodge F, Guillaso S, Jolivet R, Lasserre C, Ducret G, Grandin R, Pathier E, Pinel V (2011) Presentation of the small baseline processing chain on a case example: The Etna deformation monitoring from 2003 to 2010 using ENVISAT data. Proc. Fringe 2011, ESA, Frascati, Italy. pp. 1–7.

Dramis F, Sorriso-Valvo M (1994) Deep-seated gravitational slope deformations, related landslides and tectonics. Eng Geol 38(3–4):231–243

Ferretti A, Prati C, Rocca F (2001) Permanent scatterers in SAR interferometry. IEEE Trans Geosci Remote Sens 39:8–20

Follacci J-P (1987) Les mouvements du versant de la Clapière à Saint-Etienne-de-Tinée. Bull Liaison Lab Ponts Chaussées 150–151:39–54

Follacci J-P (1999) Seize ans de surveillance du glissement de La Clapière (Alpes Maritimes). Bull Liaison Lab Ponts Chaussées 220:35–51

Follacci J-P, Guardia P, Ivaldi J-P (1988) La Clapière landslide in its geodynamical setting. In: Bonnard C (ed) Proc. 5th Int. Symp. Landslides, vol. 3. Balkema, Brookfield, pp 1323–1327

Follacci J-P, Rochet L, Serratrice J-F (1993) Glissement de La Clapière, St. Etienne de Tinée, Synthèse des connaissances et actualisation des risques, Rapport CETE, Nice, 76pp.

Foster J, Kealy J, Cherubini T, Businger S, Lu Z, Murphy M (2013) The utility of atmospheric analyses for the mitigation of artifacts in InSAR. J Geophys Res Solid Earth 118:748–758

Fruneau B, Achache J, Delacourt C (1996) Observation and modelling of the Saint-Étienne-de-Tinée landslide using SAR interferometry. Tectonophysics 265:181–190

Girault F, Terrier M (1994) Analyse par photogrammétrie des mouvements de terrain : application aux sites de la Clapière, du Friolin, de Boulc et de l'Harmalière. Rapport BRGM, Marseille, **96pp**

Goldstein RMM, Zebker HA, Werner CL (1988) Satellite radar interferometry: two-dimensional phase unwrapping. Radio Sci 23:713–720

Guglielmi Y, Cappa F, Binet S (2005) Coupling between hydrogeology and deformation of mountainous rock slopes: insights from La Clapière area (southern Alps, France). C R Geosci 337:1154–1163

Gunzburger Y, Laumonier B (2002) Origine tectonique du pli supportant le glissement de terrain de la Clapière (Nord-Ouest du massif de l'Argentera–Mercantour, Alpes du Sud, France) d'après l'analyse de la fracturation. C. R Geosci 334:415–422

Helmstetter A, Sornette D, Grasso J-R, Andersen J, Gluzman S, Pisarenko V (2004) Slider block friction model for landslides: application to Vaiont and La Clapière landslides. J Geophys Res 109, B02409

Hradecký J, Pánek T (2008) Deep-seated gravitational slope deformations and their influence on consequent mass movements (case studies from the highest part of the Czech Carpathians). Nat Haz 45(2):235–253

Ivaldi J-P, Guardia P, Follacci J-P, Terramorsi S (1991) Plis de couverture en échelon et failles de second ordre associés à un décrochement dextre de socle sur le bord nord-ouest de l'Argentera (Alpes-Maritimes, France). C R Acad Sci II 313:61–368

Jomard H (2006) Analyse multi-échelles des déformations gravitaires du Massif de l'Argentera Mercantour. PhD Thesis, University of Nice, 268pp.

Jomard H, Lebourg T, Tric E (2007) Identification of the gravitational boundary in weathered gneiss by geophysical survey: La Clapière landslide (France). J Appl Geophys 62:47–57

Lebourg T, Binet S, Tric E, Jomard H, El Bedoui S (2005) Geophysical survey to estimate the 3D sliding surface and the 4D evolution of the water pressure on part of a deep seated landslide. Terra Nov 17:399–406

Lebourg T, Hernandez M, Zerathe S, El Bedoui S, Jomard H, Fresia B (2010) Landslides triggered factors analysed by time lapse electrical survey and multidimensional statistical approach. Eng Geol 114:238–250

Li Z, Fielding EJ, Cross P, Muller J-P (2006) Interferometric synthetic aperture radar atmospheric correction: GPS topography-dependent turbulence model. J Geophys Res Solid Earth 111, B02404

Lu P, Casagli N, Catani F, Tofani V (2012) Persistent scatterers interferometry hotspot and cluster analysis (PSI-HCA) for detection of extremely slow-moving landslides. Int J Remote Sens 33(2):466–489

Massonnet D, Feigl KL (1998) Radar interferometry and its application to changes in the Earth's surface. Rev Geophys 36:441–500

Raucoules D, De Michele M, Malet J-P, Ulrich P (2013) Time-variable 3D ground displacements from high-resolution synthetic aperture radar (SAR). Application to La Valette landslide (South French Alps). Remote Sens Environ 139:198–204

Rosen PA, Hensley S, Peltzer G, Simons M (2004) Updated repeat orbit interferometry package released. EOS Trans Am Geophys Union 85:47–47

Rott H (2009) Advances in interferometric synthetic aperture radar (InSAR). Prog Phys Geogr 33:769–791

Rott H, Nagler T (2006) The contribution of radar interferometry to the assessment of landslide hazards. Adv Sp Res 37:710–719

Schlögel R, Doubre C, Malet J-P, Masson F (2015) Landslide deformation monitoring with ALOS/PALSAR imagery: a D-InSAR geomorphological interpretation method. Geomorphology 231:314–330

Serratrice J-F (2006) Modeling of major rockfalls by spreading: application to the "La Clapière" and "Séchilienne" sites (French Alps). Bull Liaison Lab Ponts Chaussées 263–264:53–70

Squarzoni C, Delacourt C, Allemand P (2003) Nine years of spatial and temporal evolution of the La Valette landslide observed by SAR interferometry. Eng Geol 68:53–66

Stumpf A, Malet J-P, Allemand P, Ulrich P (2014) Surface reconstruction and landslide displacement measurements with Pléiades satellite images. ISPRS J Photogramm Remote Sens 95:1–12

Travelletti J, Malet J-P, Samyn K, Grandjean G, Jaboyedoff M (2013) Control of landslide retrogression by discontinuities: evidence by the integration of airborne- and ground-based geophysical information. Landslides 10:37–54

Wei M, Sandwell DT (2010) Decorrelation of L-band and C-band interferometry over vegetated areas in California. IEEE Trans Geos Remote Sens 48:2942–2952

Zhao C, Lu Z, Zhang Q, de la Fuente J (2012) Remote sensing of environment large-area landslide detection and monitoring with ALOS/PALSAR imagery data over Northern California and Southern Oregon, USA. Remote Sens Environ 124:348–359

R. Schlögel · J.-P. Malet (✉) · C. Doubre
Institut de Physique du Globe de Strasbourg, UMR7516,
Université de Strasbourg/EOST, CNRS,
5 rue René Descartes, 67084, Strasbourg, Cedex, France
e-mail: jeanphilippe.malet@unistra.fr

T. Lebourg
Géosciences Azur, CNRS UMR 6526,
Université de Nice-Sophia Antipolis,
250 Avenue A. Einstein, Valbonne, France